

Terahertz emission in the van der Waals magnet CrSiTe₃

Peng Suo¹, Wei Xia², Wenjie Zhang¹, Xiaoqing Zhu¹, Jibo Fu¹, Xian Lin¹, Zuanming Jin^{1,3}, Yongle Li¹, Weimin Liu^{2,3}, Yanfeng Guo^{2,3*} and Guohong Ma^{1,3*}

¹Department of Physics, Shanghai University, Shanghai 200444, China

²School of Physical Science and Technology, ShanghaiTech University, Shanghai 201210, China

³STU & SIOM Joint Laboratory for superintense lasers and the applications, Shanghai 201210, China

* Corresponding authors: phymagh@shu.edu.cn (G. Ma) and guoyf@shanghaitech.edu.cn (Y. Guo)

Abstract: The van der Waals magnet CrSiTe₃ has captured immense interest because it is capable of retaining the long-range ferromagnetic order even in its monolayer form, thus offering potential use in spintronic devices. Bulk CrSiTe₃ crystal is an indirect gap semiconductor with the gap size of ~ 0.4 eV at room temperature. Here, ultrafast terahertz (THz) emission spectroscopy and time resolved THz spectroscopy are employed to investigate the THz emission and the dynamics of photocarrier respectively in CrSiTe₃ crystal, it is found that the CrSiTe₃ crystal is a good candidate for THz generator with mid-IR laser pulse pumping, demonstrating by the very large second order nonlinear coefficient which is even 30 times larger than that in the conventional THz emitter, (110)-oriented ZnTe crystal. Theoretical analysis based on space symmetry of CrSiTe₃ suggests the dominant role of surface optical rectification effect in producing the THz emission, in consistence with the experimental observation that the emitted THz amplitude strongly dependents on the azimuthal and pumping polarization angles. The present study offers a new efficient THz emitter as well as a better understanding of the nonlinear optical response of CrSiTe₃. It hopefully will open a window toward the investigation on the nonlinear optical response in the mono-/few-layer van der Waals crystals with low-dimensional magnetism.

1. Introduction

The van der Waals (vdW) magnets, such as CrXTe_3 ($X = \text{Si, Ge}$), display extraordinary physical properties arising from the complex magnetic exchanges.^[1-4] One prominent virtue of this family of materials is that even in the atomically thin limit they still exhibit intrinsic long-range magnetic order which was previously thought to be strictly prohibited by thermal fluctuations in two-dimensional (2D) systems with continuous symmetry, thus offering opportunities to fundamentally study this peculiar low-dimensional magnetism and explore the potential use in spintronics.^[5-7] Furthermore, the combination of the semiconductivity and magnetism in a single material provides ideal candidate for potential applications in optoelectronics.^[8]

Most of the present attentions are paid on the magnetic properties of CrXTe_3 ,^[1-6, 9-12] while the optical properties, especially the nonlinear optical response, remain nearly uninvestigated.^[11, 13-16] In fact, as a semiconductor with narrow band gap, CrXTe_3 may exhibit optical response intimately related to the intrinsic properties. To guide the light into this shadow area, we performed study on the nonlinear optical response of the CrSiTe_3 (CST) single crystal at room temperature by employing THz emission spectroscopy combined with optical pump and THz probe (OPTP) spectroscopy.^[17-18] Interestingly, a broad band terahertz (THz) radiation upon femtosecond pulse illumination is observed, which was confirmed to arise from the surface optical rectification. The effective nonlinear coefficient in CST was found to be more than 30 times larger than that in a conventional THz emitter ZnTe. In addition, optical pump and THz probe spectroscopy measurements also reveal two relaxation processes of the photocarrier dynamics, i.e. the electron-phonon coupling and the surface defect trapping processes.

2. Experimental Results

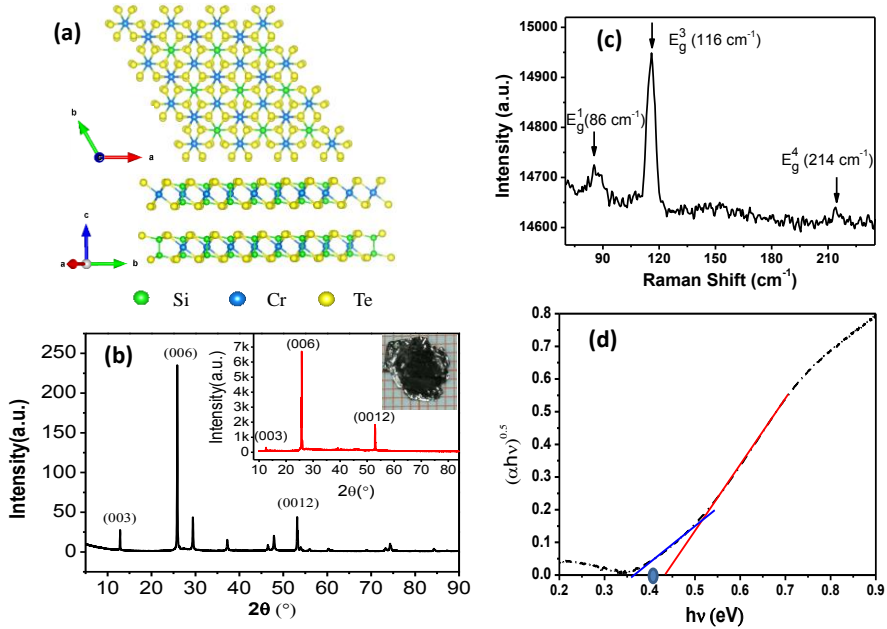


Figure 1. Structure, quality and band gap of CST single crystal. (a) Schematic crystal structures seen from different orientations (upper panel: top view, lower panel: side view). (b) Room temperature X-ray diffraction pattern of CST powder. The inset presents the XRD pattern and the picture of the *c*-cut CST single crystal. (c) Raman spectroscopy of CST single crystal with laser wavelength of 514.5 nm. (d) $(\alpha h\nu)^{0.5}$ plotted against the photo energy $h\nu$. The interceptions of the red and blue lines with the horizontal axis give the sizes for the direct and indirect band gaps, which are 1.2 and 0.4 eV, respectively.

Bulk CST crystallizes into a layered structure with each unit cell being constructed by three CST layers stacking in an *ABC* sequence, in which the short Si-Si bonds form Si pairs and hence Si_2Te_6 ethane-like groups. The Cr ions locate at the centers of slightly distorted octahedron of Te atoms. The Cr ions and Si pairs, in a 2:1 ratio, form the octahedral site plane and are sandwiched between Te planes. The crystal structure of CST is illustrated in Figure 1(a) seen along different orientations. Figure 1(b) presents the room temperature powder x-ray diffraction (XRD) pattern that could be indexed on the basis of $\bar{R}\bar{3}h$ space group. The crystal was cut along the *ab*-plane, i.e. *c*-cut, for later measurements, shown by the inserted picture in Figure 1(b). The inset also shows the XRD pattern collected on the surface of *c*-cut crystal, indicating good

crystallinity of our crystals. Figure 1(c) presents the Raman scattering of the CST single crystal at room temperature with cross polarization configuration, revealing the three Raman peaks locating at 86 cm^{-1} , 116 cm^{-1} and 145 cm^{-1} which are assigned as E_g^1 , E_g^3 and E_g^4 modes, respectively. The asymmetry profile of the most pronounced feature of E_g^3 at low temperature evidences the spin-phonon coupling in the crystal. ^[14] The absorbance, αl , is obtained by measuring the UV-visible absorption spectrum at room temperature. Figure 1(d) plots the $(\alpha h\nu)^{0.5}$ against $h\nu$, where α , h , and ν are the absorption coefficient, Planck constant, and frequency, respectively. The band gap energy, E_g , is determined to be about $0.4\pm0.03\text{ eV}$, agreeing well with the calculated value. ^[11] The band structure of CST presented in the Supplememntary Information (SI) by Figure S1 was calculated by meams of the first-principle method with VASP package,^[19] which clearly shows an indirect gap semiconductor nature at room temperature with the gap of 0.43 eV and a direct band gap of 1.20 eV . From the analysis of the indirect band gap shown in Figure 1(d), the coupling phonon energy is determined as about 100 meV , which is much larger than that of fundamental phonon modes, suggesting the important role(s) of the overtone and/or combination modes in the optical transition. ^[11]

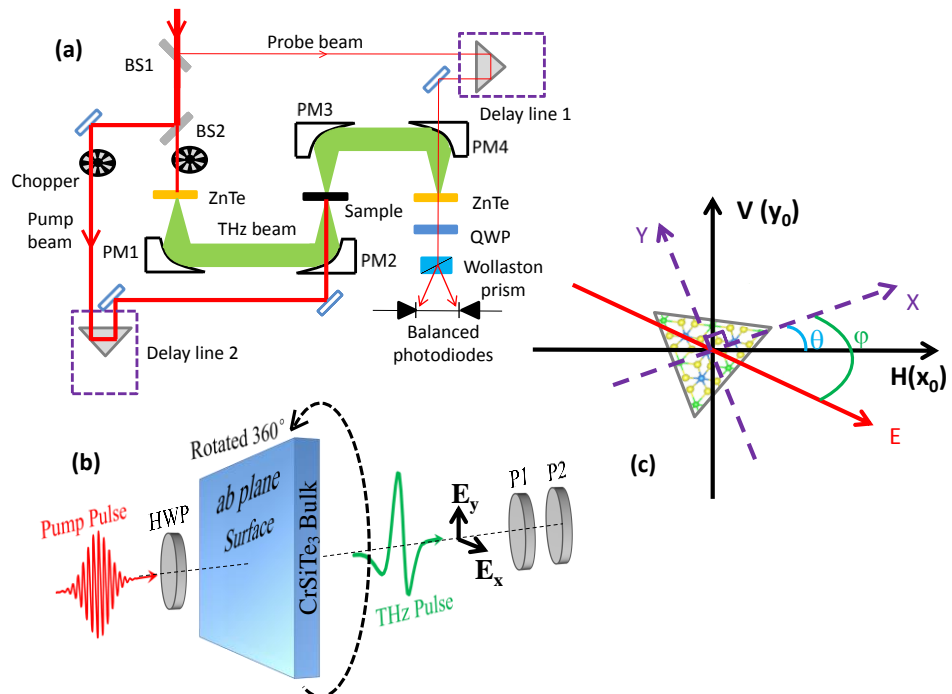


Figure 2. Experimental setups. (a) Schematics of experimental arrangements for optical pump and THz probe spectroscopy. (b) Illustration of experimental arrangement for THz emission spectroscopy, in which the THz polarizer P1 is fixed along horizontion for all measurement, P2 was placed behind P1 with polarization of $\pm 45^0$ with that of P1 during the measurement of polarization of THz radiation. (c) Illustration of relative positions of laboratory coordinate system (x_0 - y_0), sample coordinate system (x - y), as well as the direction of polarization (E) of the incident laser pulse.

Our experimental setups for THz emission and OOPTP measurements are depicted schematically in Figures 2 (a) and (b), respectively. Figure 2(c) illustrates the relative position of laboratory coordinate system (x_0 - y_0) (x_0 and y_0 are set along the horizontal (H) and vertical (V) directions, respectively), the sample coordinate system (x - y), and the polarization direction of incident laser pulse. The THz beam was enclosed and purged with dry nitrogen to avoid water vapor absorption. All measurements were performed at room temperature unless we specifically noted. As shown in Figure S2.1 in SI, CST has a refractive index of 3.17 with negligible absorption to the investigated THz frequency, therefore the THz emission spectroscopy with transmission configuration is applied, which makes the data analysis much simpler. We would like to note that the *c*-cut CST crystal shows isotropy in the THz transmission in the *ab*-plane, and is almost independent of the temperature in the investigated THz frequency, which are presented respectively in Figure S2.2 and Figgure S2.3 in SI.

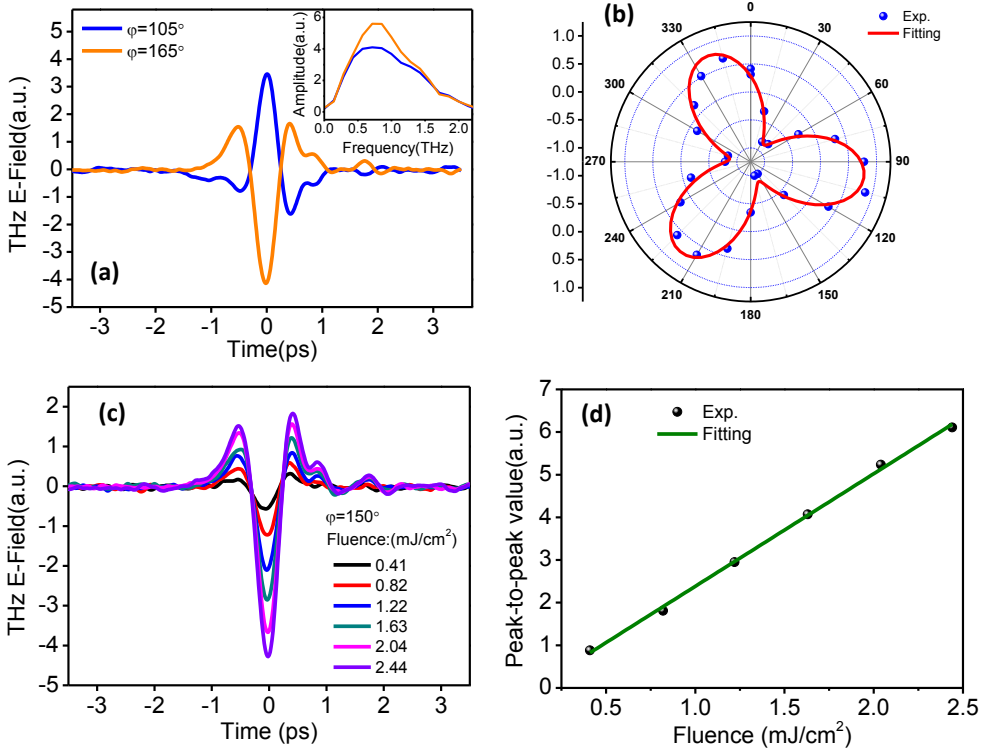


Figure 3. THz radiation of *c*-cut CST single crystal induced by femotosecond laser pulse. (a) THz emission spectra in time domain for two typical azimuthal angles, and the corresponding Fourier transformation spectra (inset of (a)). (b) The amplitude of emitted THz electric field dependence on the azimuthal angle φ , the solid line is the fitting curves with sine function. (c) The emitted THz spectra in time domain with various pump fluence, and (d) the peak-to-peak amplitude of THz radiation with respect to the pump fluence. The solid line is linear fitting.

Figure 3 displays the main results of THz radiation of the *c*-cut CST single crystal induced by femontosecond (fs) laser pulse at central wavelength of 800 nm. The absorption coefficient of CST to 800 nm laser is about $1.6 \times 10^5 \text{ cm}^{-1}$ ^[11] indicating an optical penetration depth of about 62.5 nm and the induced THz emission mainly comes from the surface effect. Figure 3(a) shows the fs pulse induced THz radiation for two selected azimuthal angles, i.e. $\varphi = 105^\circ$ and 165° , respectively. The inset in Figure 3(a) is the Fourier transformation of the data shown in the main panel. The THz emission has a broad bandwidth covering from 0.1 to 2.0 THz. The polarity of

THz emission reverses its sign when the azimuthal angle changes 60^0 . Figure 3(b) plots the azimuthal angle dependent amplitude of the generated THz electric field, it is clearly seen that the THz emission strength shows a triple symmetry, which shows a good consistence with the structural symmetry in *ab*-plane of the crystal. Figure 3(c) shows the pump fluence dependence of THz emission amplitude in time domain at the azimuthal angle of 150^0 , revealing a good linear dependence on the pump fluence as is plotted by Figure 3(d), which indicates that the THz generation is originated from the surface optical rectification effect rather than photo Dember effect as that observed in InAs semiconductor.^[20]

In order to evaluate the polarization of the THz radiation, a pair of wire-grid polarizers (P1 and P2) was placed between two parabolic mirrors, PM3 and PM4, as illustrated in Figure 2(b), in which the polarization of P1 is fixed along horizontal direction, and P2 is aligned at polarization angle of $\pm 45^0$ with respect to the horizontal direction. The sum and difference of these two spectra at $\pm 45^0$ give the horizontal and vertical electric-field components, respectively.^[21-22] Our experiment confirmed that the THz waveform obtained from the sum signals between $+45^0$ and -45^0 agrees well with the waveform measured directly at the horizontal component. Figure 4(a) presents the measured magnitudes of horizontal (E_H) and vertical (E_V) components of THz radiation with respect to the azimuthal angle φ . the amplitude of either E_H or E_V changes with φ with a periodicity of 120^0 , consistent with the theoretical prediction based on optical rectification model given later and harmonious with the triple symmetry in the *ab*-plane of CST. The solid lines in Figure 4(a) are fitting curves with sine function, which give the phase retardation between E_H and E_V of about 33^0 that is close to the theoretical value of $\pi/6$ given later. Figures 4 (b) and (c) present the three-dimensional (3D) plots of the generated THz polarization at $\varphi = 0^0$ and 30^0 , respectively. The polarization of THz radiation changes from horizontal with $\varphi = 0^0$ to vertical with $\varphi = 30^0$, which does support the conclusion that φ dependent amplitude

of THz radiation shows three periodicities in the range of $\varphi = 0^0$ to 2π . More experimental data are presented in Figure S3 of the SI.

Next, we investigated the pump polarization dependence of THz radiation with the fixed angle, θ . The pump polarization can be changed continuously by rotating a half-wave plate (HWP) inserted in the pump path. Figure 4 (d) shows the peak-to-peak amplitude of E_H and E_V components of THz radiation with respect to φ . The peaking amplitude oscillates with φ in a periodicity of 180^0 . The solid lines are the fitting curves with sine function, which produces the phase retardation between E_H and E_V of about 50^0 , closed to the theoretical value of $\pi/4$ as presented later. Figures 4(e) and (f) present the 3D plots of the polarization of THz radiation at $\varphi = 0^0$ and 45^0 , respectively, showing that the polarization of THz radiation changes from horizontal with $\varphi = 0^0$ to vertical with $\varphi = 45^0$. The result is in support of that φ dependent amplitude of THz radiation shows two periodicities in the range of $\varphi = 0$ to 2π . More experimental data about the 3D plots of the polarization of THz radiation with polarization angle changing from 0^0 to 300^0 are presented in Figure S4 of the SI.

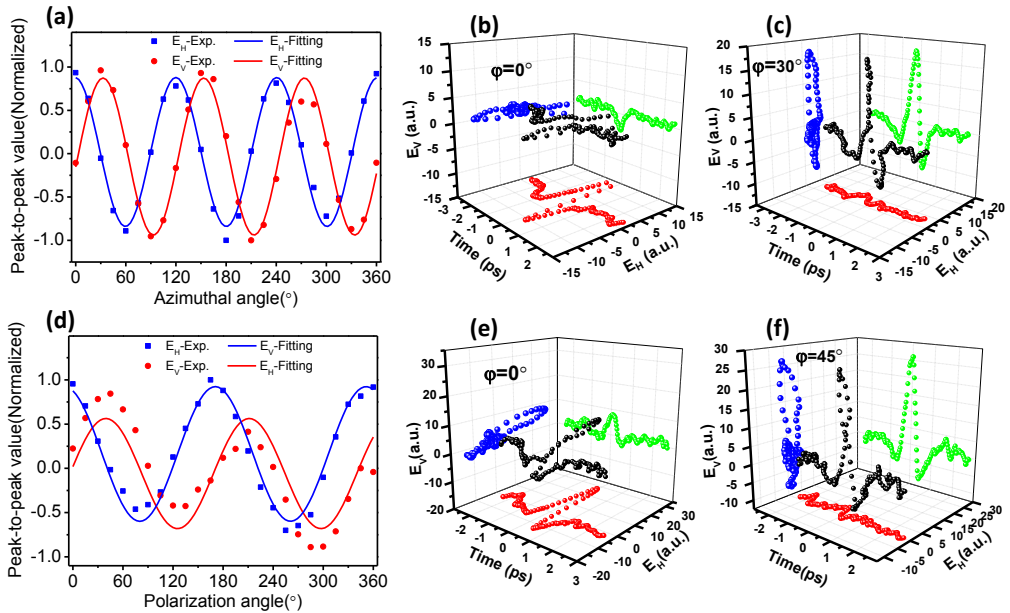


Figure 4. (a) Peak-to-peak amplitude of horizontal (E_H) and vertical (E_V) components of THz radiation with respect to the azimuthal angle from 0 to 2π , the solid lines are fitting curves with Eqs. (5) and (6). 3D plots of THz radiation with two selected

azimuthal angles $\varphi=0^0$ (b) and 30^0 (c). (d) Peak-to-peak amplitude of horizontal (E_H) and vertical (E_V) components of THz radiation with respect to the polarization angle φ with fixed θ , the solid lines are fitting curves with Eqs.(7) and (8). 3D plots of THz radiation with two selected polarization angles $\varphi=0^0$ (e) and 45^0 (f).

As illustrated in Figure 2(c), the x-y system is assigned as a sample coordinate system, in which the angle θ is the included angle between x and x_0 . The \mathbf{E} is the polarization direction of incident optical pulse and the azimuthal angle φ denotes the angle between x and \mathbf{E} . The fs pulse propagating along z(c)-axis of the CST crystal generates the THz emission. Supposing that the generated THz wave (with electric field \vec{E}_{THz} , the arrow denotes the vector character) is a plane wave and the wave equation in the crystal can be written as ^[23-24]

$$\frac{\partial^2 \vec{E}_{THz}(z, \Omega)}{\partial z^2} + \epsilon(\Omega) \frac{\Omega^2}{c_0^2} \vec{E}_{THz}(z, \Omega) = -\Omega^2 \mu_0 \vec{P}^{(OR)}(z, \Omega) \quad (1)$$

where Ω and $\epsilon(\Omega)$ are angular frequency and dielectric constant of CST crystal in the THz band, $\vec{P}^{(OR)}$ denotes the second order polarization in CST crystal via optical rectification, c_0 and μ_0 are the speed of light in vacuum and the permeability of the crystal at room temperature (CST is considered as a paramagnetic material at room temperature), respectively. Considering the light intensity of ultrafast pulses with the Gaussian time envelope, $I_{pu}(t) = E_0^2 \exp(-2t^2 / \tau_p^2)$ with the pulse duration of τ_p , the second order nonlinear polarization of optical rectification effect in right term of Eq. (1) is

$$\vec{P}^{(OR)}(z, \Omega) = \frac{\vec{d}_{eff}(\Omega) C(\Omega)}{\pi} \exp(i\Omega z / V_{opt}) \quad (2)$$

where \vec{d}_{eff} denotes the effective nonlinear coefficient, which depends on the azimuthal (polarization) angle φ , $C(\Omega)$ is the Fourier transformation of the optical pump pulse $I_{pu}(t)$, V_{opt} is the optical group velocity in the CST crystal. Using slowly varying envelope approximation, solution of Eq. (1) can be expressed as

$$\vec{E}_{THz}(z, \Omega) \propto z \frac{E_0^2 \Omega^2 \vec{d}_{eff} C(\Omega)}{8c_0^2 k(\Omega)} \sin c \left(\frac{\Omega}{c_0} (n_{Opt} - n_{THz}) \frac{z}{2} \right) \quad (3)$$

where $k(\Omega)$ is a module of the wave vector in THz frequency, n_{THz} and c_0 are THz refractive index of the crystal and the velocity of light in free space.

The THz wave generation efficiency is dominated by two factors: one is the phase mismatching factor, $\frac{\Omega}{c_0} (n_{Opt} - n_{THz})$, which in fact depends on the refractive index difference between THz frequency and optical frequency, i.e. $n_{Opt} - n_{THz}$. The THz wave generation efficiency is maximal when $n_{Opt} = n_{THz}$ which is the phase matching condition. The penetration depth of CST at 800 nm is about 62.5 nm, which is three-order of magnitude smaller than the walk off length l_w ($l_w \sim 61 \mu\text{m}$, SI), so that the sinc function in the right term of Eq. (3) is approaching one. The magnitude of effective nonlinear coefficient, \vec{d}_{eff} , which in sample coordinate frame can be expressed as (refer to the SI for details):

$$\vec{d}_{eff} = (d_{11} \cos 2\varphi + d_{16} \sin 2\varphi) \vec{x} + (-d_{16} \cos 2\varphi + d_{11} \sin 2\varphi) \vec{y} + d_{31} \vec{z} \quad (4)$$

where φ denotes the azimuthal angle or polarization angle.

When the pump polarization is fixed along x_0 -axis (horizontal) in laboratory coordinate, the generated THz electric field components E_H^{THz} and E_V^{THz} with respect to the azimuthal angle φ is (refer to the SI for details):

$$E_H^{THz} \sim E_x^{THz} \cos \varphi - E_y^{THz} \sin \varphi \propto \sqrt{d_{11}^2 + d_{16}^2} \sin(3\varphi + \Phi) \quad (5)$$

1.

$$\text{and } E_V^{THz} \sim E_x^{THz} \sin \varphi + E_y^{THz} \cos \varphi \propto \sqrt{d_{11}^2 + d_{16}^2} \sin\left(3(\varphi + \frac{\pi}{6}) + \Phi\right) \quad (6)$$

where $\Phi = \tan^{-1}(d_{11}/d_{16})$. The generated THz E -field, E_{THz} , as a function of azimuthal angle φ is proportional to $\sin(3\varphi + \Phi)$. The solid lines in Figure 3(b) are fitting curves by using Eqs. (5) and (6), showing a nice consistence between experimental data and simulation. By comparing Eqs. (5) and (6), the phase difference between E_H and E_V in each period is easily found to be 30° . The solid lines in Figure 3(d) are the fitting

curves with sine function, which produce the phase difference of 33^0 between the two curves, close to the theoretical value predicted by Eqs.(5) and (6).

When sample position is fixed, i.e. θ remains unchanged, the incident polarization \mathbf{E} of optical pulse is changed by rotating a half-wave plate. The horizontal and vertical components of the generated THz electric field are (refre to the SI for details):

$$E_H^{THz} \sim E_x^{THz} \cos \theta - E_y^{THz} \sin \theta \propto \sqrt{d_{11}^2 + d_{16}^2} \sin(2\varphi + \theta + \Phi) \quad (7)$$

and

$$E_V^{THz} \sim E_x^{THz} \sin \theta + E_y^{THz} \cos \theta \propto \sqrt{d_{11}^2 + d_{16}^2} \sin\left(2(\varphi + \frac{\pi}{4}) + \theta + \Phi\right) \quad (8)$$

with $\Phi = \tan^{-1}(d_{11}/d_{16})$. It is clearly seen from Eqs. (7) and (8) that the magnitude of THz field changes periodically with polarization angle φ in the relation of $\sin(2\varphi + \theta + \Phi)$. From Eqs. (7) and (8), it is also clear that the phase difference between horizontal and vertical directions is $\pi/4$ in each periodicity. Solid lines in Figre 4 are the fitted curves with Eqs. (7) and (8), revealing a good agreement between experimental data and simulation.

3. Discussions

By referring to optical parameters of (110)-oriented ZnTe, the absolute value of the THz electric field in CST can be calculated according to the current measurement with Lock-in amplifier [25-26]:

$$\frac{\Delta I}{I_{probe}} = \frac{\omega n^3 E_{THz} r_{41} L}{c} \quad (9)$$

where the nonzero electro-optic coefficient $r_{41} = 3.9$ pm/V of ZnTe, the refractive index n of ZnTe is 2.8 at 800 nm, the ω is the circular frequency, the length of the crystal $L = 1$ mm, ΔI and I_{probe} denote the THz electric field induced intensity change of probe beam in ZnTe and the probe beam intensity, respectively. The peak amplitude of $\Delta I/I_{probe}$ is measured to be 2×10^{-4} , and the peak value of THz electric

field generated in CST is calculated to be about 29.8 V/cm based on Eq. (9). The effective nonlinear coefficient in CST crystal could be more than 30 times larger than that of ZnTe with considering the ~ 62.5 nm optical penetration depth at 800 nm. In addition, the CST crystal is transparent and dispersion-free in the frequency range of 0.1 to 2.5 THz, making it a good candidate as a THz emitter with mid-IR pump if the phase matching condition (i.e. $n_{THz} = n_{optics}$) could be satisfied.

Considering the used photon energy of 1.55 eV in our experiment is even larger than the size of direct band gap, 1.2 eV, not to mention the size of indirect band gap, 0.4 eV, the photoinduced surface current therefore can also contribute to the THz emission.^[27-30] In order to eliminate this effect, we also performed measurement by using circular polarization of fs laser pulse. The results presented in Fig. S6 of the SI clearly show that the THz emission in such case is too weak to be observable.

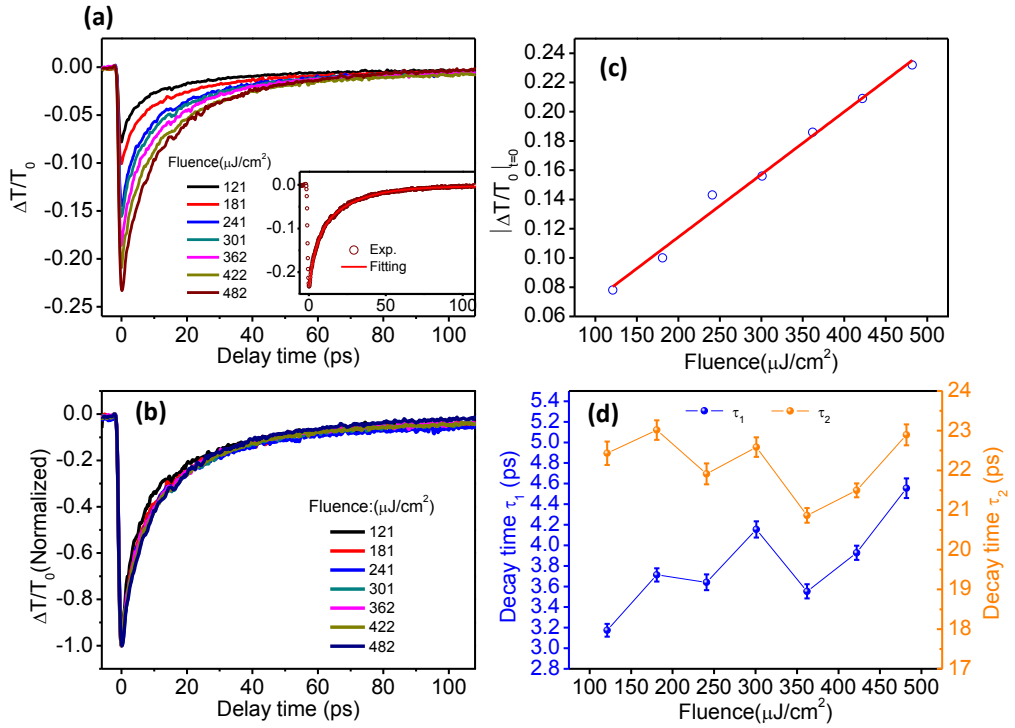


Figure 5. Transient THz transmission in CrSiTe_3 . (a) Transient THz transmission under various pump fluences at a wavelength of 800 nm. The inset shows the fitting curve (under pump fluence of 141 $\mu\text{J}/\text{cm}^2$) with bi-exponential function. (b) The normalized transient THz transmission with various pump fluence (normalization of

(a)). (c) $|\Delta T/T_0|$ at zero delay time is plotted with respect to pump fluence. (d) The magnitudes of fitting time constant (τ_1 and τ_2) under various pump fluences.

Another possible source producing the THz emission is the transient photocarrier dynamics resulted from the above photoexcitation at 800 nm.^[31-32] In such case, it is expected that transient dynamics of photocarrier should display ultrafast response with subpicosecond lifetime. Figure 5(a) presents the transient THz transmission under various pump fluences, which shows that the dynamics of relaxation could be well reproduced with bi-exponential function, where the red curve in inset of Figure 5(a) denotes the fitting result of one transient response to the pump fluence of $482 \mu\text{J}/\text{cm}^2$. The normalized transient THz transmission under various pump fluences is presented in Figure 5(b), showing that all curves follow an identical relaxation process. Figure 5(c) plots the peak transmission change at zero delay time, $(\Delta T/T_0)_{\Delta t=0}$, with respect to the pump fluence, which displays a good linear relationship, indicating that no saturable effect until the highest pump fluence of $482 \mu\text{J}/\text{cm}^2$. With bi-exponential fitting, Figure 5(d) displays the pump fluence dependent fitting lifetimes. It is clear that the fast component increases slightly with pump fluence while the magnitude of τ increases very fast from 3.0 ps at $121 \mu\text{J}/\text{cm}^2$ to 4.0 ps at $482 \mu\text{J}/\text{cm}^2$. The slow component has a constant lifetime of 23 ± 3 ps, nearly independent of the pump fluence. We assigned tentatively the fast relaxation as the electron-phonon coupling and the slow one as the surface defect-mediated electron-hole recombination process. The absence of the subpicosecond relaxation process thus could exclude the transient photocarrier effect as the origin of the observed THz emission and confirm the dominated role of the optical rectification.

4. Conclusions

To summarize, by performing fs laser pulse illumination on the high-quazlity CrSiTe_3 single crystal, a broad band THz emission is observed, which increases linearly in strength with increasing the pump pulse intensity. Our analysis on the measurements

suggests that the THz emission is induced by the surface optical rectification effect. The effective nonlinear coefficient in CrSiTe_3 is more than 30 times larger than that of a conventional THz emitter, the ZnTe crystal, indicating that CrSiTe_3 is a good candidate for THz emitter. Furthermore, optical pump and THz probe experimental reveals that the photocarrier relaxation follows two processes, the fast process with lifetime of a few ps increases slightly with the pump fluence, which is assigned as the electron-phonon coupling process. The slow component with lifetime 23 ± 3 ps comes from the phonon-mediated electron-hole recombination. Our experimental results not only have demonstrated for the first time the ultrafast nonlinear optical response in this type of bulk layered 2D magnet, but also provide a good candidate for THz emitter with high conversion efficiency.

Experimental Section

CrSiTe_3 single crystal growth. The CrSiTe_3 single crystals were grown using a self-flux method. Starting materials of Cr powder (99.999% Alfa Aesar), Si (99.999%, Alfa Aesar) and Te (99.9999%, Alfa Aesar) blocks thorogly mixed in a molar ratio of 1:2:6 were placed into an alumina crucible. The crucible was tehn sealed in a quartz tube in vaccum and was heated up to 1150 °C within 15 hrs in a furnace, held at this temperature for 20 hrs, and subsequently cooled down to 800 °C at a rate of 1.5 °C/h. After staying at 800 °C for more than 5 hours, The excess Si and Te was quickly removed at this temperature in a centrifuge and black crystals with shining surface were finally left . The as-grown crystals are plate-like with the in-plane dimension of ~ 8 mm in diameter.

Optical pump and THz probe spectroscopy. Figure 2(a) schematically shows the experimental arrangement of optical pump THz probe spectroscopy. The laser beam delivered from Ti: sapphire laser, with a center wavelength of 800 nm, repetition rate of 1 kHz and pulse duration of 120 fs, is split into three beams. The first one is used for ultrafast optical pump. The THz pulses, co-propagating with the pump pulse, is

generated by optical rectification and detected by electro-optic sampling in a pair of (110)-oriented ZnTe crystals with the thickness of 1.0 mm, by the other two beams. The spot size of the THz beam on the sample position is 2.0 mm, whereas the spot size of the pump beam on the sample is 6.5 mm, and the large pump spot size ensures a relatively uniform photoexcited region for THz probe.

THz emission spectroscopy. THz emission spectroscopy is similar as that of Figure 2(a) with the pump beam was blocked and the emitted ZnTe was replaced by CrSiTe₃ crystal. As shown schematically in Figure 2(b), the *c*-cut CrSiTe₃ crystal is irradiated at normal incidence with weakly focused beam. The 120-fs-pulse-duration is much shorter than the period of the emitted THz bursts, enabling the coherent emission. The THz detection system is based on electro-optic sampling with a 1 mm thick (110)-oriented ZnTe crystal. As illustrated in Fig. 2(c), the CrSiTe₃ crystal was mounted onto a stage that can rotate in vertical plane for adjusting azimuthal angle (ϕ). A half-wave plate was placed before the CrSiTe₃ crystal, which is used to change the polarization angle (ϕ) of incident laser pulse (see Figure 2(c)). A pair of THz polarizers, P1 and P2, were placed between two parabolic mirrors, PM3 and PM4, as illustrated in Fig. 2(a), which was used to measure the horizontal and vertical polarization of the emitted THz radiation, respectively.

Data availability. The data that support the plots within this paper and other findings of this study are available from the corresponding authors upon reasonable request.

Acknowledgements: This work is supported by the National Natural Science Foundation of China (NSFC, Nos. 11674213, 11604202, 61735010, 11874264), the Natural Science Foundation of Shanghai (Grant No. 17ZR1443300). Z.J. thanks Shanghai Municipal Education Commission (Young Eastern Scholar QD2015020), Science and Technology Commission of Shanghai Municipality (Shanghai Rising-Star Program 18QA1401700). Y.F.G. acknowledges the support by the ShanghaiTech University startup fund.

References

- [1] N. Sivadas, M. W. Daniels, R. H. Swendsen, S. Okamoto, and D. Xiao, Phys. Rev. B **2015**, 91, 235425.
- [2] C. Gong, L. Li, Z. Li, H. Ji, A. Stern, Y. Xia, T. Cao, W. Bao, C. Wang, Y. Wang, Z. Q. Qiu, R. J. Cava, S. G. Louie, J. Xia, X. Zhang, Nature **2017**, 546, 265.
- [3] B. Huang, G. Clark, E. Navarro-Moratalla, D. R. Klein, R. Cheng, K. L. Seyler, D. Zhong, E. Schmidgall, M. A. McGuire, D. H. Cobden, W. Yao, D. Xiao, P. Jarillo-Herrero, and X. D. Xu, Nature **2017**, 546, 270.
- [4] H. Li, S. C. Ruan, Y. J. Zeng, Adv. Mater. **2019**, 31, 1900065.
- [5] D. R. Klein, D. MacNeill, J. L. Lado, D. Soriano, E. Navarro-Moratalla, K. Watanabe, T. Taniguchi, S. Manni6, P. Canfield, J. Fernández-Rossier, P. Jarillo-Herrero, Science **2018**, 360, 1218-1222.
- [6] L. Thiel, Z. Wang, M. A. Tschudin, D. Rohner, I. Gutiérrez-Lezama, N. Ubrig, M. Gibertini, E. Giannini2 A. F. Morpurgo, P. Maletinsky, Science **2019**, 364, 973–976.
- [7] J. X. Zhang, X. C. Cai, W. Xia, A. J. Liang, J. W. Huang, C. W. Wang, L. X. Yang, H. T. Yuan, Y. L. Chen, S. L. Zhang, Y. F. Guo, Z. K. Liu, G. Li, Phys. Rev. Lett. **2019**, 123, 047203.
- [8] C. Gong, X. Zhang, Science **2019**, 363, eaav4450.
- [9] Z. T. Zhang, Z. H. Wang, Z. D. Zhang, Appl. Phys. Lett. **2018**, 113, 142404.
- [10] Y. Liu and C. Petrovic, Phys. Rev. Mater. **2019**, 3, 014001.
- [11] L. D. Casto, A. J. Clune, M. O. Yokosuk, J. L. Musfeldt, T. J. Williams, H. L. Zhuang, M.-W. Lin, K. Xiao, R. G. Hennig, B. C. Sales, J.-Q. Yan, and D. Mandrus, APL Mater. **2015**, 3, 041515.
- [12] K. Y. Wang, T. Hu, F. H. Jia, G. D. Zhao, Y. Y. Liu, I. V. Solovyev, A. P. Pyatakov, A. K. Zvezdin, and W. Ren, Appl. Phys. Lett. **2019**, 114, 092405.
- [13] W. C. Jin, H. H. Kim, Z. P. Ye, S. W. Li, P. Y. Rezaie, F. B. Diaz, S. Siddiq, E. Wauer, B. W. Yang, C. H. Li, S. J. Tian, K. Sun, H. C. Lei, A. W. Tsen, L. Y. Zhao, and R. He, Nat. Comm. **2018**, 9, 5122.
- [14] A. Milosavljevic, A. Solajic, J. Pesic, Y. Liu, C. Petrovic, N. Lazarevic, and Z. V. Popovic, Phys. Rev. B **2018**, 98, 104306.

- [15] Y. Kim and J. D. Lee, *Phys. Rev. B* **2018**, 97, 041105(R).
- [16] A. Autere, H. Jussila, Y. Y. Dai, Y. D. Wang, H. Lipsanen, Z. P. Sun, *Adv. Mater.* **2018**, 1705963.
- [17] P. Han, X. K. Wang, Y. Zhang, *Adv. Opt. Mater.* **2019**, 1900533.
- [18] P. Gopalan, B. Sensale-Rodriguez, *Adv. Opt. Mater.* **2019**, 1900550.
- [19] G. T. Lin, H. L. Zhuang, X. Luo, B. J. Liu, F. C. Chen, J. Yan, Y. Sun, J. Zhou, W. J. Lu, P. Tong, Z. G. Sheng, Z. Qu, W. H. Song, X. B. Zhu, and Y. P. Sun, *Phys. Rev. B* **2017**, 95, 245212.
- [20] P. Gu, M. Tani, *Terahertz Optoelectronics*, Springer: Berlin, **2005**; pp 63–98.
- [21] M. Nakajima, A. Namai, S. Ohkoshi, and T. Suemoto, *Opt. Express* **2010**, 18, 18260.
- [22] J. J. Jiang, Z. M. Jin, G. B. Song, X. Lin, G. H. Ma, and S. X. Cao, *Appl. Phys. Lett.* **2013**, 103, 062403.
- [23] D. Li, and G. H. Ma, *J. Appl. Phys.* **2008**, 103, 123101.
- [24] J.-P. Caumes, L. Videau, C. Rouyer, and E. Freysz, *Phys. Rev. Lett.* **2002**, 89, 047401.
- [25] Y. Y. Huang, L. P. Zhu, Q. Y. Zhao, Y. H. Guo, Z. Y. Ren, J. T. Bai, and X. L. Xu, *ACS Appl. Mater. Interfaces* **2017**, 9, 4956.
- [26] P. C. M. Planken, H.-K. Nienhuys, H. J. Bakker, T. Wenckebach, *J. Opt. Soc. Am. B* **2001**, 18, 313.
- [27] X. B. Wang, L. Cheng, D. P. Zhu, Y. Wu, M. J. Chen, Y. Wang, D. M. Zhao, C. B. Boothroyd, Y. M. Lam, J.-X. Zhu, M. Battiato, J. C. W. Song, H. Yang, and E. E. M. Chia, *Adv. Mater.* **2018**, 30, 1802356.
- [28] Y. Gao, Y. Qin, S. Kaushik, E. J. Philip, Y. P. Liu, Y. L. Su, X. Chen, Z. Li, H. Weng, D. E. Kharzeev, M. K. Liu, and J. Q, arXiv: 1901.00986.v3.
- [29] N. Sirica, R. I. Tobey, L. X. Zhao, G. F. Chen, B. Xu, R. Yang, B. Shen, D. A. Yarotski, P. Bowlan, S. A. Trugman, J.-X. Zhu, Y. M. Dai, A. K. Azad, N. Ni, X. G. Qiu, A. J. Taylor, and R. P. Prasankumar, *Phys. Rev. Lett.* **2019**, 122, 197401.
- [30] F. Nastos, and J. E. Sipe, *Phys. Rev. B* **2006**, 74, 035201.

[31] L. Braun, G. Mussler, A. Hruban, M. Konczykowski, T. Schumann, M. Wolf, M. Münzenberg, L. Perfetti, T. Kampfrath, *Nat. Commun.* **2016**, 7, 13259.

[32] J. M. Schleicher, S. M. Harrel, C. A. Schmuttenmaera, *J. Appl. Phys.* **2009**, 105, 113116.

Supplementary Information

Terahertz emission in the van der Waals magnet CrSiTe₃

Peng Suo¹, Wei Xia², Wenjie Zhang¹, Xiaoqing Zhu¹, Jibo Fu¹, Xian Lin¹, Zuanming Jin^{1,3,4}, Yongle Li¹, Weimin Liu^{2,3}, Yanfeng Guo^{2,3} and Guohong Ma^{1,3*}*

¹Department of Physics, Shanghai University, Shanghai 200444, China

²School of Physical Science and Technology, ShanghaiTech University, Shanghai 201210, China

³STU & SIOM Joint Laboratory for superintense lasers and the applications, Shanghai 201210, China

* Corresponding authors: phymagh@shu.edu.cn (G. Ma) and guoyf@shanghaitech.edu.cn (Y. Guo)

1. The calculated band structure and density of states for CST single crystal

All first-principle electronic structure calculations were performed using the Vienna *ab initio* simulation package (VASP), with the projector augmented wave (PAW) method of Perdew–Burke–Ernzerhof (PBE) functional to treat the interactions between the valence-electrons and their inner core. A plane-wave basis set along with energy cutoff of 450 eV is used to describe electron wavefunctions. A $4 \times 4 \times 1$ Monkhorst-Pack grid has been employed to sample the Brillouin zone. During the simulations, both the lattice constants and positions of all atoms are relaxed until the force is less than 0.01 eV \AA^{-1} . The criterion for the total energy is set as 1×10^{-6} eV. To confirm the validity of our method, the lattice constants of bulk CST are optimized to be $a = 6.837 \text{ \AA}$, $c = 20.599 \text{ \AA}$. Calculated crystallographic properties obtained by relaxing the structures are in good agreement with previous reports. [1-2]

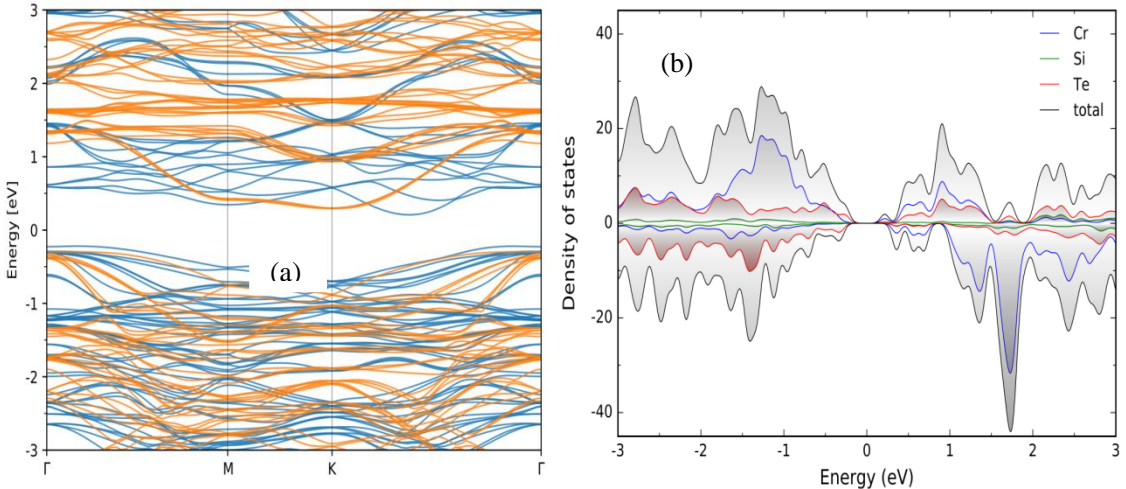


Figure S1. The calculated band structure (a) and density of states (b) of CST single crystal with VASP.

2. Refractive index of CST in THz frequency and the temperature dependent THz transmission

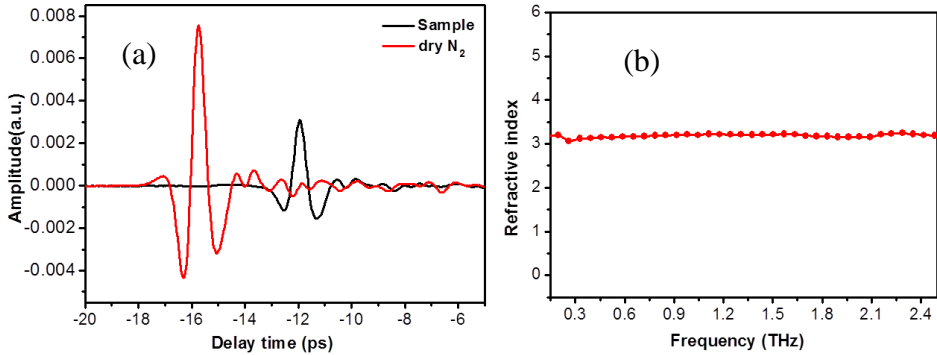


Figure S2.1. (a) THz time domain transmission spectra of dry nitrogen and CrSiTe₃ single crystal with thickness of 0.43 mm. (b) the refractive index dispersion of CrSiTe₃ crystal in frequency range from 0.2 to 2.5 THz, and the average index of fraction is about 3.17.

In addition, we also measured the transmitted THz polarization change with respect to the azimuthal angle, which is presented in Figure S.2.2. It is clearly seen that the THz polarization does not show any observable change with rotating the sample's azimuthal angle from 0 to 180°, indicating that the property of the *ab*-plane for the *c*-cut CST crystal is isotropic.

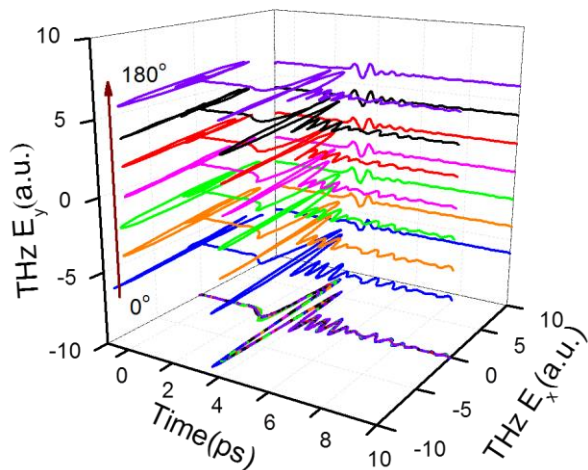


Figure S2.2. A 3D plot of THz transmission of CrSiTe₃ crystal with respect to the azimuthal angle at room temperature.

Temperature dependent THz transmission in CST crystal.

It is noted that the CST crystal undergoes a ferromagnetic ordering around $T_C = 33$ K [2]. In order to exclude the influence of phase transition on the THz transmission spectra, Figure S3 shows the temperature dependent THz transmission spectra, it is clear that the THz transmission is nearly temperature independence in temperature range of 5 - 300 K.

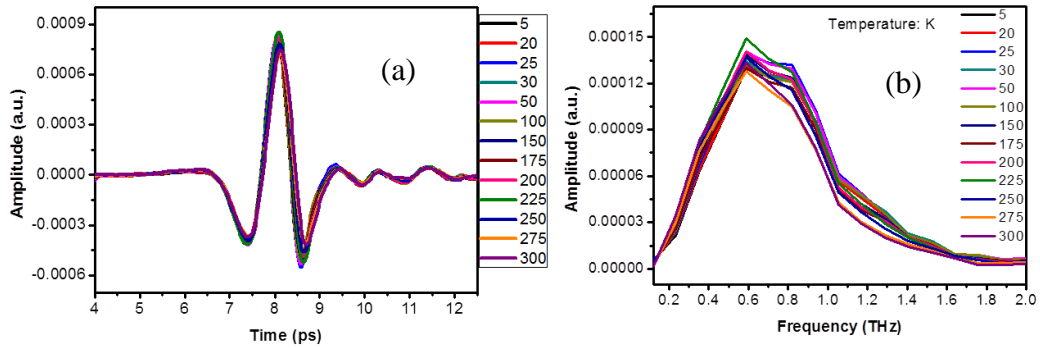


Figure S2.3 THz transmission in time domain (a) and in frequency domain (b) with Fourier transformation in temperature range from 5 K to 300 K.

3. The 3D plots of emitted THz polarization with respect to the azimuthal angle

Both horizontal (E_H) and vertical (E_V) polarization changes of the THz emission with respect to the azimuthal angle can be evaluated by using a pair of THz polarizer. With rotating the c-cut CST crystal around z-axis with angle φ , Figure S4 presents the 3D plots of the THz radiation.

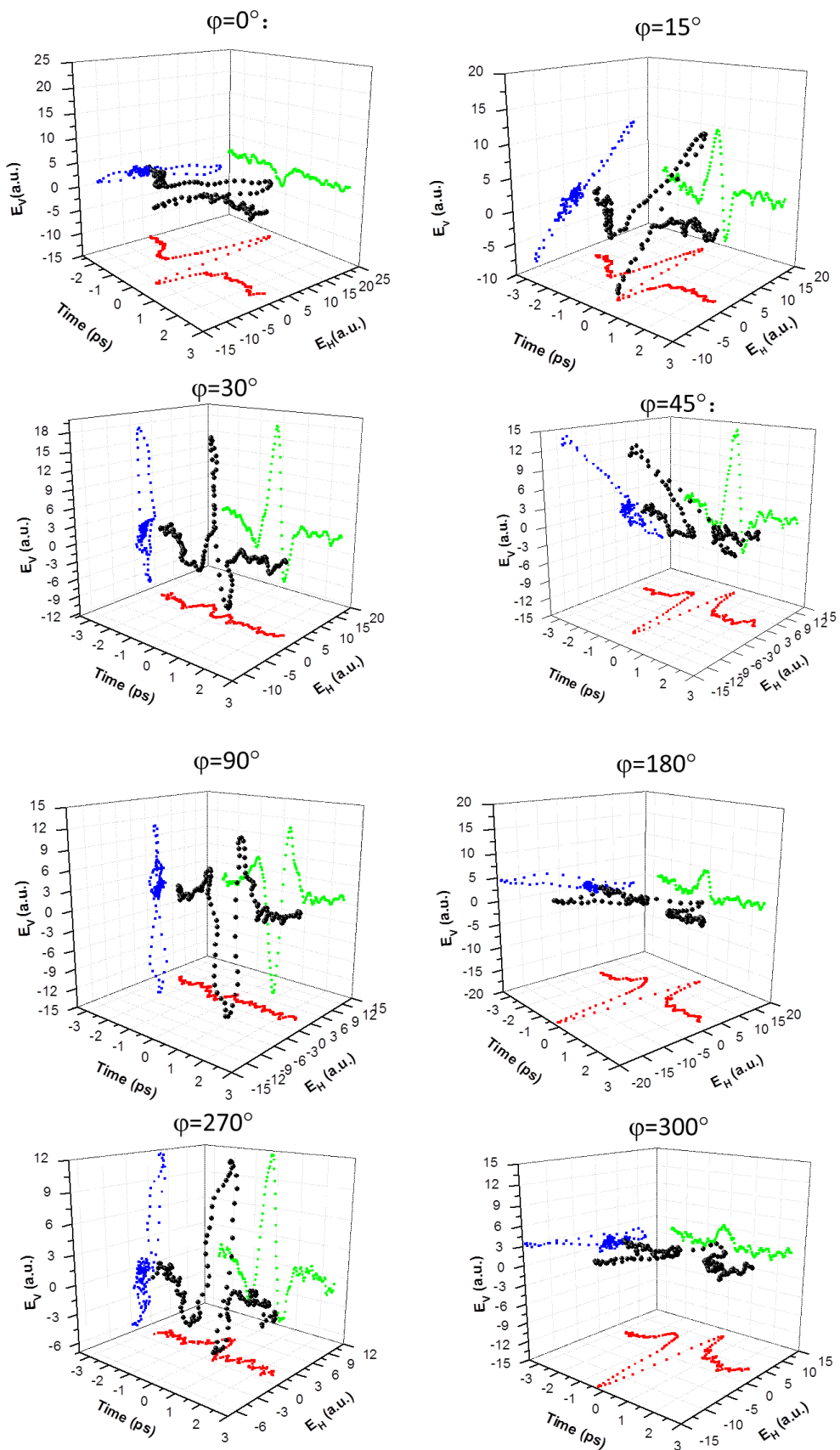
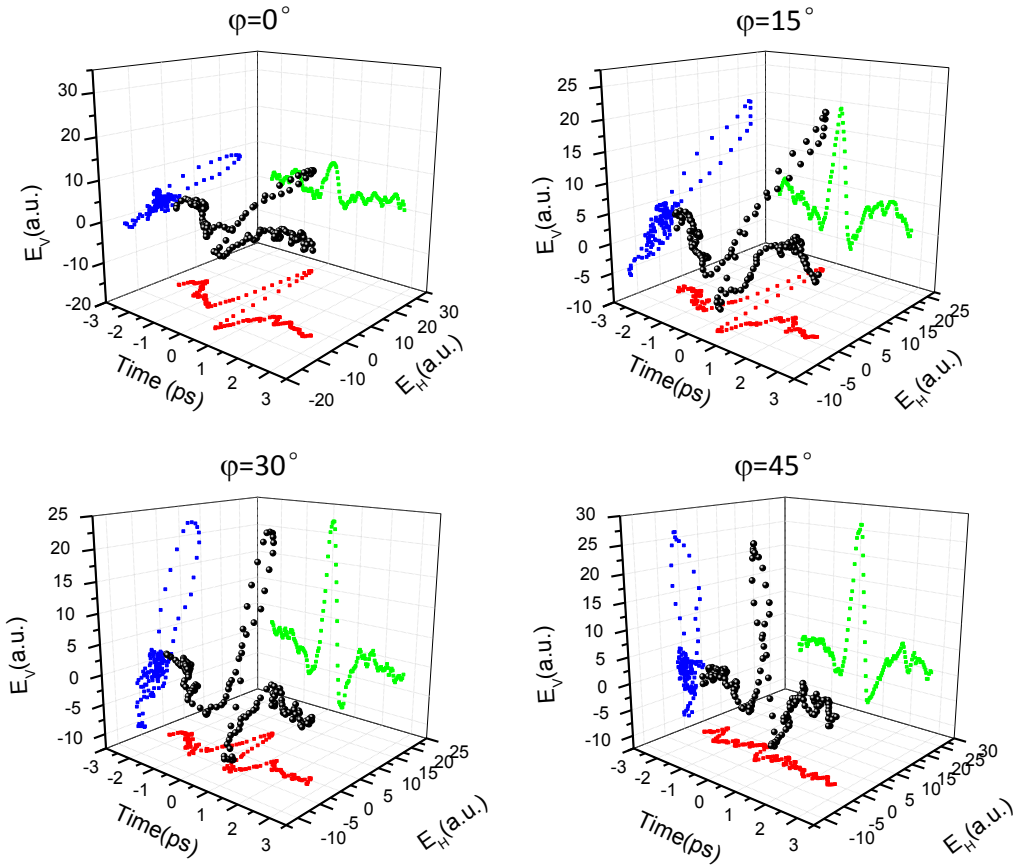


Figure S3. The 3D plots of the polarization of the THz emission with respect to the azimuthal angle φ .

4. The 3D plot of emitted THz polarization with respect to the polarization angle

When the sample position is fixed, we changed the pump polarization by rotating a half wave plate in optical path of pump beam, so that both E_H and E_V polarization changes of the THz emission with respect to the polarization angle is obtained by using a pair of THz polarizer. With changing the pump polarization angle φ , Figure S5 presents the 3D plots of the THz radiation.



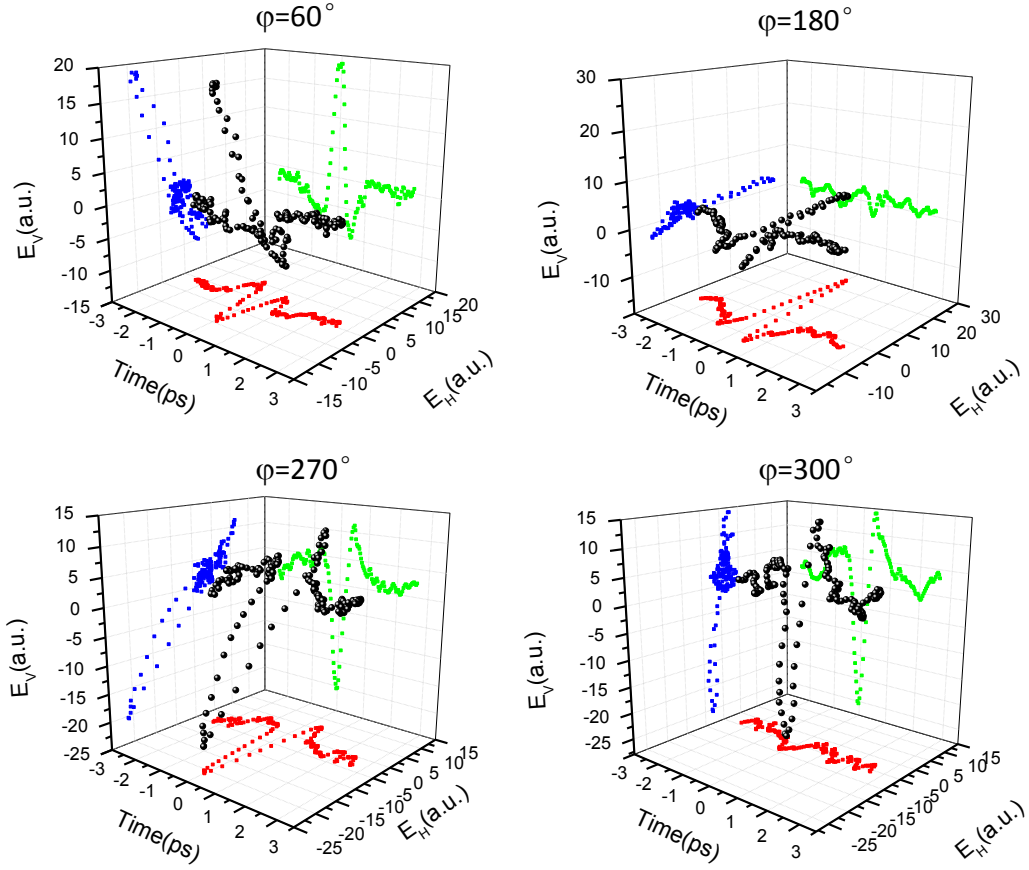


Figure S4. The 3D plots of the polarization of the THz emission with respect to the polarization angle φ .

5. The evaluation of walking-off length in CST single crystal.

The walking off length l_w between optical pulse and generated THz radiation can be evaluated with following formula: [3]

$$l_w = \frac{C\tau_p}{n_{THz} - n_{Opt}} \quad (S1)$$

where C and τ_p are the speed of light at vacuum and optical pulse duration, respectively. n_{THz} and n_{Opt} denote the refractive indices of CST crystal at THz and optical frequency, respectively. In the present case, the fs laser pulse has pulse duration of $\tau_p = 120$ fs, the n_{THz} is measured to be 3.17 in the investigated frequency range from 0.2 to 2.5 THz, while n_{Opt} is determined to be about 2.5 around 800 nm. Therefore, the walking-off length (l_w) is calculated to be about 61 μm , which is three-order longer than the penetration depth (62.5 nm) at 800 nm.

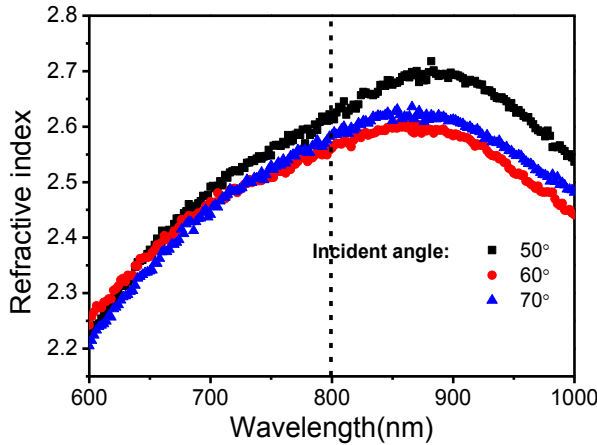


Figure S5. Refractive index dispersion obtained from optical ellipsometer with three incident angles in the wavelength range from 600 nm to 1000 nm, the average refractive index around 800 nm of the sample is determined to be 2.58.

6. Details for obtaining the effective nonlinear coefficient.

6.1 Derivation of the effective nonlinear coefficient d_{eff} ,

The single crystal CST can be indexed as $R\bar{3}$ space group with a C_{3i} point group, the second order nonlinear susceptibility, in form of d-matrix, can be written as:

$$\begin{pmatrix} d_{11} & -d_{11} & 0 & d_{14} & d_{15} & -d_{16} \\ -d_{16} & d_{16} & 0 & d_{15} & -d_{14} & -d_{11} \\ d_{31} & d_{31} & d_{33} & 0 & 0 & 0 \end{pmatrix} \quad (S2)$$

The femtosecond laser pulse is incident along c -axis of the crystal, φ is the azimuthal angle, defined as the angle between the optical electric field and the x-axis of the crystal, and the optical field \vec{E} can be written as a 1×3 matrix,

$$\vec{E} = E_0 \begin{pmatrix} \cos \varphi \\ -\sin \varphi \\ 0 \end{pmatrix} \quad (S)$$

The pump laser pulse is written as $I_{pu}(t) = E_0^2 \exp(-2t^2 / T^2)$, with E_0 representing the amplitude of incident laser pulse. Then the nonlinear optical polarization for optical rectification $\mathbf{P}^{(\text{OR})}$ can be expressed as:

$$\begin{aligned}
\begin{pmatrix} p_x^{(\text{OR})} \\ p_y^{(\text{OR})} \\ p_z^{(\text{OR})} \end{pmatrix} &= 2\epsilon_0 E_0^2 \begin{pmatrix} d_{11} & -d_{11} & 0 & d_{14} & d_{15} & -d_{16} \\ -d_{16} & d_{16} & 0 & d_{15} & -d_{14} & -d_{11} \\ d_{31} & d_{31} & d_{33} & 0 & 0 & 0 \end{pmatrix} \begin{pmatrix} \sin^2 \varphi \\ \cos^2 \varphi \\ 0 \\ 0 \\ 0 \\ -2\sin \varphi \cos \varphi \end{pmatrix} \\
&= 2\epsilon_0 E_0^2 \begin{pmatrix} -d_{11} \cos 2\varphi - d_{16} \sin 2\varphi \\ d_{16} \cos 2\varphi - d_{11} \sin 2\varphi \\ d_{31} \end{pmatrix} \quad (S4)
\end{aligned}$$

Under phase matching condition, the effective nonlinear coefficient in sample coordinate system, \vec{d}_{eff} is then obtained as

$$\vec{d}_{eff} = (d_{11} \cos 2\varphi + d_{16} \sin 2\varphi) \vec{x} + (-d_{16} \cos 2\varphi + d_{11} \sin 2\varphi) \vec{y} + d_{31} \vec{z} \quad (S5)$$

6.2 Derivation of azimuthal angle dependent E_H and E_V component of THz radiation

Here, the polarization of optical pulse is set horizontally, therefore we have $\varphi = 0$.

The E_H and E_V component of THz radiation then is

$$\begin{aligned}
E_H &= E_x \cos \theta - E_y \sin \theta = E_x \cos \varphi - E_y \sin \varphi \\
&\sim [(d_{11} \cos 2\varphi + d_{16} \sin 2\varphi) \cos \varphi - (-d_{16} \cos 2\varphi + d_{11} \sin 2\varphi) \sin \varphi] \\
&= [d_{11} \cos 2\varphi \cos \varphi + d_{16} \sin 2\varphi \cos \varphi + d_{16} \cos 2\varphi \sin \varphi - d_{11} \sin 2\varphi \sin \varphi] \\
&= [d_{11} (\cos 2\varphi \cos \varphi - \sin 2\varphi \sin \varphi) + d_{16} (\sin 2\varphi \cos \varphi + \cos 2\varphi \sin \varphi)] \\
&= [d_{11} \cos(2\varphi + \varphi) + d_{16} \sin(2\varphi + \varphi)] \\
&= [d_{11} \cos 3\varphi + d_{16} \sin 3\varphi] \\
&= \sqrt{d_{11}^2 + d_{16}^2} \sin(3\varphi + \Phi) \quad (S6)
\end{aligned}$$

$$\begin{aligned}
E_V &= E_x \sin \theta + E_y \cos \theta = E_x \sin \varphi + E_y \cos \varphi \\
&\sim [(d_{11} \cos 2\varphi + d_{16} \sin 2\varphi) \sin \varphi + (-d_{16} \cos 2\varphi + d_{11} \sin 2\varphi) \cos \varphi] \\
&= [d_{11} \cos 2\varphi \sin \varphi + d_{16} \sin 2\varphi \sin \varphi - d_{16} \cos 2\varphi \cos \varphi + d_{11} \sin 2\varphi \cos \varphi] \\
&= [d_{11} (\cos 2\varphi \sin \varphi + \sin 2\varphi \cos \varphi) + d_{16} (\sin 2\varphi \sin \varphi - \cos 2\varphi \cos \varphi)] \\
&= [d_{11} \sin(2\varphi + \varphi) - d_{16} \cos(2\varphi + \varphi)] \\
&= [d_{11} \sin 3\varphi - d_{16} \cos 3\varphi] \\
&= -\sqrt{d_{11}^2 + d_{16}^2} \cos(3\varphi + \Phi) = \sqrt{d_{11}^2 + d_{16}^2} \cos(3\varphi + \Phi + \pi) \\
&= \sqrt{d_{11}^2 + d_{16}^2} \sin\left(3(\varphi + \frac{\pi}{6}) + \Phi\right)
\end{aligned} \tag{S7}$$

wher $\Phi = \tan^{-1}(d_{11}/d_{16})$.

6.3 Derivation of pump polarization dependent E_H and E_V components of THz emission

The included angle φ denotes the angle between the the polarization of pump pulse and the x-axis of the crystal, which is changed by a half-wave plate. As illustrated in Figure 2(c), the angle θ is fixed at this situation. The E_H and E_V component of THz radiation is then,

$$\begin{aligned}
E_H &= E_x \cos \theta - E_y \sin \theta \\
&\propto (d_{11} \cos 2\varphi + d_{16} \sin 2\varphi) \cos \theta - (-d_{16} \cos 2\varphi + d_{11} \sin 2\varphi) \sin \theta \\
&\propto d_{11} (\cos 2\varphi \cos \theta - \sin 2\varphi \sin \theta) + d_{16} (\sin 2\varphi \cos \theta + \cos 2\varphi \sin \theta) \\
&\propto d_{11} \cos(2\varphi + \theta) + d_{16} \sin(2\varphi + \theta) \\
&\propto \sqrt{d_{11}^2 + d_{16}^2} \sin(2\varphi + \theta + \Phi)
\end{aligned} \tag{S8}$$

$$\begin{aligned}
E_V &= E_x \sin \theta + E_y \cos \theta \\
&\propto (d_{11} \cos 2\varphi + d_{16} \sin 2\varphi) \sin \theta + (-d_{16} \cos 2\varphi + d_{11} \sin 2\varphi) \cos \theta \\
&= d_{11} \sin(2\varphi + \theta) - d_{16} \cos(2\varphi + \theta) \\
&= -\sqrt{d_{11}^2 + d_{16}^2} \cos(2\varphi + \theta + \Phi) \\
&= \sqrt{d_{11}^2 + d_{16}^2} \sin(2(\varphi + \frac{\pi}{4}) + \theta + \Phi)
\end{aligned} \tag{S9}$$

where $\Phi = \tan^{-1}(d_{11}/d_{16})$.

7. THz emission with circular pump polarization

We also conducted the THz emission measurement with circular polarization of pump beam, which is shown in Figure S6. It is clearly seen that THz emission shows negligible signal with that of linear case, which reveals that pump induced charge current contribution to the THz radiation is too weak to be ignored. If we look carefully at the THz emission with circular polarization, it is noted that THz emission with right-handed circular polarization (RCP) shows out of phase with that of left-handed circular polarization (LCP).

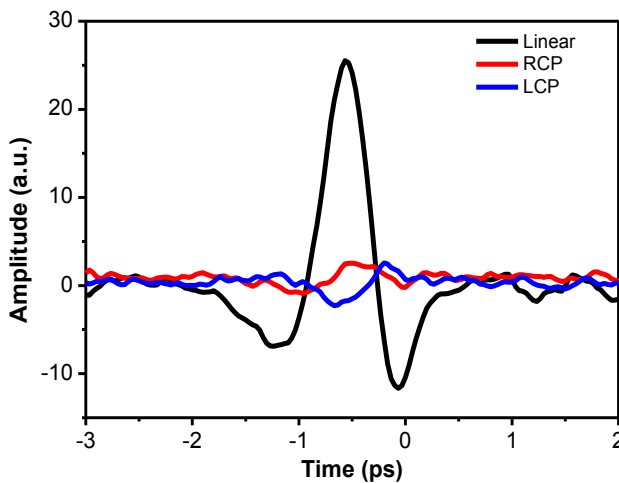


Figure S6. THz emission in time domain under 800 nm pump with linear (black), right-handed circular polarization (red) and left-handed circular polarization (blue), respectively.

References

- [1] Naohiro Ito, Takashi Kikkawa, Joseph Barker, Daichi Hirobe, Yuki Shiomi, and Eiji Saitoh. Spin Seebeck effect in the layered ferromagnetic insulators CrSiTe₃ and CrGeTe₃, *Phys. Rev. B* 100, 060402(R) (2019).
- [2] L. D. Casto, A. J. Clune, M. O. Yokosuk, J. L. Musfeldt, T. J. Williams, H. L. Zhuang, M.-W. Lin, K. Xiao, R. G. Hennig, B. C. Sales, J.-Q. Yan, and D. Mandrus, Strong spin-lattice coupling in CrSiTe₃, *APL Mater.* **2015**, 3, 041515.
- [3] Kai-Erik Peiponen, J. Axel Zeitler, Makoto Kuwata-Gonokami, *Terahertz Spectroscopy and Imaging*, Springer (2013).